Journal of Neurochemistry

JOURNAL OF NEUROCHEMISTRY | 2017 | 140 | 404–420 doi: 10.1111/jnc.13891

ORIGINAL ARTICLE

Margatoxin-bound quantum dots as a novel inhibitor of the voltage-gated ion channel Kv1.3

Austin B. Schwartz,* Anshika Kapur,† Wentao Wang,† Zhenbo Huang,‡ Erminia Fardone,‡,§ Goutam Palui,† Hedi Mattoussi† and Debra Ann Fadool*,‡,§

*Institute of Molecular Biophysics, Florida State University, Tallahassee, Florida, USA
†Department of Chemistry and Biochemistry, Florida State University, Tallahassee, Florida, USA
‡Program in Neuroscience, Florida State University, Tallahassee, Florida, USA
§Department of Biological Science, Florida State University, Tallahassee, Florida, USA

Abstract

Venom-derived ion channel inhibitors have strong channel selectivity, potency, and stability; however, tracking delivery to their target can be challenging. Herein, we utilized luminescent quantum dots (QDs) conjugated to margatoxin (MgTx) as a traceable vehicle to target a voltage-dependent potassium channel, Kv1.3, which has a select distribution and well-characterized role in immunity, glucose metabolism, and sensory ability. We screened both unconjugated (MgTx) and conjugated MgTx (QD-MgTx) for their ability to inhibit *Shaker* channels Kv1.1 to Kv1.7 using patch-clamp electrophysiology in HEK293 cells. Our data indicate that MgTx inhibits 79% of the outward current in Kv1.3-transfected cells and that the QD-MgTx conjugate is able to achieve a similar level of block, albeit a slightly reduced efficacy (66%) and at a slower time course (50% block by 10.9 ± 1.1 min, MgTx; vs. 15.3 ± 1.2 min, QD-MgTx). Like the unbound peptide, the QD-MgTx conjugate inhibits both Kv1.3 and Kv1.2 at a 1 nM concentration, whereas it does not inhibit other screened *Shaker* channels. We tested the ability of QD-MgTx to inhibit native Kv1.3 expressed in the mouse olfactory bulb (OB). In brain slices of the OB, the conjugate acted similarly to MgTx to inhibit Kv1.3, causing an increased action potential firing frequency attributed to decreased intraburst duration rather than interspike interval. Our data demonstrate a retention of known biophysical properties associated with block of the vestibule of Kv1.3 by QD-MgTx conjugate compared to that of MgTx, inferring QDs could provide a useful tool to deliver ion channel inhibitors to targeted tissues *in vivo*.

Keywords: K channel, MgTx, nanoparticle, patch clamp, pore blocker, potassium channel.
J. Neurochem. (2017) **140**, 404–420.

Much of the known structure of voltage-gated ion channels was derived from the pharmacological probing of the vestibule of the channel long before the crystal structure was sought and solved (Catterall 1988; Mathie *et al.* 1998; Kaczorowski and Garcia 1999; Yu *et al.* 2005; Isacoff *et al.* 2013). Dating from Armstrong's first exploration of potassium (K) channels using tetraethylammonium (TEA) (Armstrong 1966, 1969) a wealth of known inhibitors for K channels emerged for a variety of therapeutic and experimental purposes (Cook 1988; Pongs 1992; Camerino *et al.* 2007). Blocking the activity of K channels through the pore vestibule has been shown to lessen health complications

Received September 3, 2016; revised manuscript received October 24, 2016; accepted October 31, 2016.

Address correspondence and reprint requests to Debra Ann Fadool, Florida State University, 319 Stadium Drive, KIN Life Science Building, Suite 3008, Department of Biological Science, Program in Neuroscience and Molecular Biophysics, Tallahassee, FL 32306, USA. E-mail: dfadool@bio.fsu.edu

Abbreviation used: κ, slope of voltage dependence; τ_{deact}, deactivation time constant; τ_{inact}, inactivation time constant; A_1, A_2, weight of the time constants in the Boltzmann Equation; ACSF, artificial cerebral spinal fluid; AVMA, American Veterinary Medicine Association; CMV, cytomegalovirus; FSU, Florida State University; HEK293, human embryonic kidney 293; IACUC, Institutional Animal Care and Use Committee; I_i, initial current; I_n, current peak amplitude at pulse number (n) for a given time "t" in minutes; Kv1.3$^{-/-}$, gene-targeted deletion of Kv1.3; Kv1.3, voltage-dependent potassium channel 1.3; Kv, voltage-dependent potassium channel; MgTx, margatoxin; min, minutes; mM, millimolar; NIH, National Institutes of Health; OB, olfactory bulb; PBS, phosphate-buffered saline; P_d, pulse duration; QD-MgTx, quantum dot conjugated margatoxin; QD, quantum dot; RT, room temperature; T, time; $V_{1/2}$, voltage at half-activation; V_c, command voltage; V_h, holding voltage.

© 2016 International Society for Neurochemistry,

resulting from CNS neuronal disorders, chronic renal failure, cardiac arrhythmia, diabetes, asthma, inflammation, and autoimmune diseases (Kazama 2015; Rubaiy 2016; Skibsbye and Ravens 2016; Yang and Nerbonne 2016). Having the ability to concentrate and track ion channel inhibitors, therefore, provides an advantage for targeted delivery of such molecules to well-characterized, voltage-gated ion channels and the concomitant regulation of excitability to mitigate disease. Herein, we utilized luminescent quantum dots (QDs) conjugated to a pore-blocking peptide as a traceable vehicle to target a delayer rectifier, voltage-dependent potassium channel, Kv1.3, which has a select distribution (Kues and Wunder 1992), and well-characterized role in immunity, glucose metabolism, and sensory ability (Fadool *et al.* 2004; Lam and Wulff 2011; Upadhyay *et al.* 2013; Chhabra *et al.* 2014; Koshy *et al.* 2014; Xie *et al.* 2015).

Kv1.3 is a mammalian homolog of the *Shaker* subfamily that classically serves to stabilize the resting potential and time the inter-spike interval in excitable neurons (Yellen 2002; Jan and Jan 2012). Kv1.3 has a select distribution within the CNS where it is expressed in the mitral cells of the olfactory bulb (OB), the principal cells of the pyriform cortex, and within the dentate gyrus of the hippocampus (Kues and Wunder 1992; Fadool and Levitan 1998; Fadool *et al.* 2000; Trimmer 2015). Kv1.3 is also an important signaling step in a variety of autoimmune diseases through triggering T-lymphocyte activation in multiple sclerosis, arthritis, and chronic respiratory problems (Rangaraju *et al.* 2009; Beeton *et al.* 2011; Lam and Wulff 2011; Chi *et al.* 2012; Toldi *et al.* 2013; Koshy *et al.* 2014). Mice with a gene-targeted deletion of Kv1.3 ($Kv1.3^{-/-}$) have an unusual phenotype that encompasses both metabolism and sensory processes (Xu *et al.* 2003; Fadool *et al.* 2004). The mice have an enhanced olfactory ability in terms of both odor discrimination and threshold (referred to as Super-smeller mice), and have increased expression of G-protein-coupled odorant receptors and G_{olf} (Fadool *et al.* 2004; Biju *et al.* 2008). They also have increased firing frequency of mitral cells in the olfactory bulb stemming from a slightly shifted membrane potential (Fadool *et al.* 2011). Cumulatively, the $Kv1.3^{-/-}$ mice are thinner than their wild-type counterparts without caloric restriction, are resistant to diet- and genetic-induced obesity, and have an increased total energy expenditure in the dark cycle (Xu *et al.* 2003, 2004; Fadool *et al.* 2004; Tucker *et al.* 2008, 2012a,b; Thiebaud *et al.* 2014). Owing to the ability for Kv1.3 channel to serve as a metabolic target to balance body weight and simultaneously enhance olfactory ability, we took advantage of known peptide blockers of this channel to investigate the feasibility of targeting QD-conjugates to Kv1.3 in human embryonic kidney 293 (HEK293) cells and mouse OB slices.

Owing to their selectivity, potency, and stability, venom-derived ion channel inhibitors make amenable drug candidates (Pineda *et al.* 2014; Kalia *et al.* 2015; Undheim *et al.* 2015). We focused our efforts upon the venom-derived peptide, margatoxin (MgTx), because of its noted robust thermal stability (Garcia-Calvo *et al.* 1993) and the ease for which we predicted it could be conjugated to QDs. MgTx is a 39 amino acid peptide derived from the venom of *Centruroides margaritatus* with an IC_{50} of 11.7 pM against Kv1.3 (Garcia-Calvo *et al.* 1993; Knaus *et al.* 1995; Bartok *et al.* 2014). We and others have demonstrated the ability of MgTx to block Kv1.3 using a variety of heterologous systems and native cells (Garcia-Calvo *et al.* 1993; Spencer *et al.* 1997; Fadool and Levitan 1998; Ghanshani *et al.* 2000; Colley *et al.* 2004; Menteyne *et al.* 2009; Fadool *et al.* 2011; Mast and Fadool 2012a; Jang *et al.* 2015). A variety of other venom-derived ion channel inhibitors are being used in clinical trials for autoimmune diseases and the treatment of pain, for example (Hagen *et al.* 2007, 2008, 2011; Beeton *et al.* 2011; Chi *et al.* 2012; Yang *et al.* 2013). Like MgTx, these molecules have high selectivity by targeting the vestibule of the channel, however, targeting to a specific location can be problematic.

There are a variety of different types of nanoparticles that can aid in delivery toward a target of interest, including luminescent quantum dots (QDs). Luminescent QDs made of CdSe–ZnS core-shell nanocrystals have unique optical and spectroscopic properties (Mattoussi *et al.* 2012). Others have designed peptide inhibitors with fluorescent tags, however, binding peptides to QDs affords the ability to concentrate the peptide on the QD surface as well as provides the advantage to conjugate multiple, different peptides to a single QD (Susumu *et al.* 2009). Molecules that increase penetration through cell or epithelial membranes can also be co-bound to the nanoparticle along with the drug or inhibitor of interest (Guo *et al.* 2016; Sheng *et al.* 2016). Dihydrolipoic acid is a ligand with strong affinity for ZnS overcoated QDs. When dihydrolipoic acid is appended with polyethylene glycol (PEG), either inert or chemically reactive (including carboxy, amine, or azide), it yields QDs that are stable over a broad range of pH and are biocompatible (Palui *et al.* 2012a,b). MgTx has many free amine groups, thus we utilized its structural chemistry to our advantage.

We developed a protocol using carbodiimide coupling chemistry (EDC/NHS) for effective conjugation of the peptide MgTx to QDs, such that this conjugate could be used to label cells expressing Kv1.3. To better understand the selectivity of the new conjugate, we screened both unconjugated (MgTx) and quantum dot-conjugated margatoxin (QD-MgTx) for their ability to block *Shaker* family members Kv1.1 to Kv1.7. We honed our electrophysiological analysis to Kv1.3 in native OB slices where we explored predicted changes in excitability induced by block of Kv1.3 conductance for neurons that are well characterized to carry a large proportion of the outward current via Kv1.3 (Fadool and Levitan 1998; Colley *et al.*

2004; Fadool *et al.* 2004). Our data demonstrate a retention of known biophysical properties associated with block of the vestibule of Kv1.3 by MgTx compared to that of the conjugated nanoparticle (QD-MgTx), as well as retention of QD properties following conjugation. These data infer that nanoparticle conjugates are potential tools to deliver ion channel inhibitors to targeted tissues *in vivo*.

Materials and methods

Ethical approval

All animal experiments were approved by the Florida State University (FSU) Institutional Animal Care and Use Committee under protocol #1427 and were conducted in accordance with the American Veterinary Medicine Association and the National Institutes of Health. For preparation of OB slices, mice were anesthetized with isoflurane (Aerrane, Baxter, Deerfield, IL, USA) using the Institutional Animal Care and Use Committee-approved drop method and were then killed by decapitation (American Veterinary Medicine Association Guidelines on Euthanasia, June 2007).

Animal care

All mice (C57BL/6J background strain; The Jackson Laboratory, Bar Harbor, ME, USA) were singly housed in conventional style open cages at the FSU vivarium on a standard 12 h/12 h light/dark cycle and were allowed *ad libitum* access to 5001 Purina Chow (Purina, Richmond, VA, USA) and water. Mice of both sexes at postnatal days 15–30 (body weight ranged from 5.6 to 14.2 g) were used for slice electrophysiology experiments.

Solutions and reagents

Phosphate-buffered salines (PBS) for conjugation (pH 6.5, 7.9) and immunocytochemistry (pH 7.4) were prepared as previously described (Clyner 2007; Biju *et al.* 2008). The bath and pipette solutions for the electrophysiology experiments using HEK293 cells were prepared as previously reported (Cook and Fadool 2002). The artificial cerebrospinal fluid (ACSF), sucrose-modified ACSF, and intracellular pipette solution for slice electrophysiology experiments were carefully monitored for osmolarity and prepared as previously reported (Fadool *et al.* 2011; Tucker *et al.* 2013; Thiebaud *et al.* 2016). All salts and sugars were purchased from Sigma-Aldrich (St Louis, MO, USA) or Fisher Scientific (Pittsburgh, PA, USA). MgTx (#M8437; Sigma Aldrich) was reconstituted in PBS to 1 μM with 0.01% bovine serum albumin and stored as stocks at −20°C. On the day of the experiment, the stock solution was diluted in either HEK293 pipette solution or ACSF, for recording cell-attached macroscopic currents from HEK293 cells or action potential firing frequency in a current-clamp configuration from OB slices, respectively. Final working concentration of MgTx back-filled in the pipette was 1 nM.

Quantum dot (QD) growth, phase transfer, and conjugation

The luminescent QDs used in this study were made of CdSe–ZnS core-shell nanocrystals, had an overall inorganic core-shell diameter of ~ 6 nm, and emitted in the red region of the visible spectrum (peak at 633 nm) (Yu and Peng 2002; Clapp *et al.* 2006). These nanocrystals were grown stepwise, starting with the core, followed by ZnS over-coating, using high-temperature reduction of cadmium, selenium, zinc, and sulfur precursors in coordinating solvent mixtures made of alkylphosphines, alkyphosphine-carboxyl, and alkylamines, following the protocols described in previous reports (Yu and Peng 2002; Clapp *et al.* 2006). The native capping ligands, made of a mixture that included trioctylphosphine/trioctylphosphine oxide (TOP/TOPO) and alkyl carboxy, were exchanged with polyethylene glycol-appended lipoic acid (LA-PEG) to promote the dispersion of the QDs in buffer media. The phase transfer strategy relied on the photochemical ligation of LA-PEG (oxidized form) combined with competitive displacement of the native ligands. Importantly, the phase transfer allowed for the introduction of a controllable fraction of reactive groups on the QD surface via mixed ligand exchange (Susumu *et al.* 2007). This permitted covalent coupling of MgTx peptide onto the QDs. In particular, QDs photoligated with 10% LA-PEG-COOH were coupled to the amine groups available on the MgTx via a 1-ethyl-2-(-dimethylaminopropyl)-carbodiimide)/N-hydroxysuccinimide (EDC/NHS) condensation reaction (Hermanson 2013). Additional details on the phase transfer, conjugation steps, and purification of the conjugate can be found in previous reports (Susumu *et al.* 2007; Palui *et al.* 2012a). The final concentration of the QD or QD-MgTx dispersion was determined from the absorbance value at 350 nm, using an extinction coefficient of the QDs (e.g., 350 nm = 2.467×10^{-6} per M/cm) (Leatherdale *et al.* 2002). The number of MgTx per QD conjugate (i.e., valence ~ 15) was estimated from the reaction conditions (reagent concentration) and assuming 75% efficiency of the EDC condensation reaction (Hermanson 2013). The QD-MgTx conjugates were stored at 4°C until the day of use. Final working concentration of QD-MgTx, back-filled in the pipette for cell-attached recordings, was 10 nM.

cDNA constructs

All *Shaker* channel coding regions were downstream from a cytomegalovirus promoter. rKv1.3 channel was subcloned into the multiple cloning region of $pcDNA_3$ (Invitrogen, Carlsbad, CA, USA) at the unique *HindIII* restriction site as previously described (Holmes *et al.* 1996). The eGFP-rKv1.3 construct (GFP-Kv1.3) was generously donated by Jürgen Kupper (Kupper 1998) and subcloned into $pcDNA_3$ by the FSU Molecular Core Facility taking advantage of the same *HindIII* sites as above (Spear *et al.* 2015). rKv1.1 and rKv1.2 constructs were generously provided by Dr. James Trimmer (University of California Davis, Davis, CA, USA) and were independently subcloned into the $pcDNA_3$ vector between the *BamHI* and *HindIII* restriction sites of the multiple cloning region. rKv1.4 and rKv1.5 cDNA were both expressed in $pcDNA_3$ and were a generous gift from Todd Holmes (University of California Irvine, Irvine, CA, USA) (Nitabach *et al.* 2002). hKv1.6 ($pcDNA_3$) and rKv1.7 (pEGFP-C3) constructs were donated by Dr. Heike Wulff (University of California Davis). pCDM8 was a kind gift from Dr. Brian Seed (Harvard University, Boston, MA, USA) (Jurman *et al.* 1994). DNA-encoding human CD8 was amplified from pCDM8 and subcloned into the $pcDNA_3$ vector between the *BamH1* and *EcoR1* restriction sites (Mast *et al.* 2010).

Maintenance, transfection, and electrophysiology of HEK293 cells

HEK293 cells were grown in Modified Eagle's Medium (#12360-038; Life Technologies/Gibco, Grand Island, NY, USA) supplemented with 2% penicillin/streptomycin (#P0781) and 10% fetal

bovine serum (#16000-044). Plating to low density and transfection procedures were carried out as previously described (Cook and Fadool 2002). Briefly, when cells reached 70–80% confluency they were transiently cotransfected with 1 μg *Shaker* cDNA plus 0.2 μg pCDM8 for 4 h using lipofectamine (#18324-012; Life Technologies/Invitrogen) in serum-reduced media (#31985-070) (Mast and Fadool 2012). Twenty-four to thirty-six hours post-transfection, cells were incubated with Dynabeads® CD8 microparticles (#11147D; Life Technologies/Gibco) for 2 min to visualize channel-transfected cells (Mast and Fadool 2012). Hoffman modulation contrast optics were used to visualize cells at 40× magnification (Axiovert 135; Carl Zeiss, Thornwood, NY, USA). Patch electrodes were fabricated from Jencons (M15/10; Jencons Limited, Bedfordshire, UK) or Sutter glass (BF150-86-15; Sutter Instrument Co., Novato, CA, USA) using a vertical puller (Model PP-830; Narishige, Tokyo, Japan). Tips were fire polished with a microforge (Model MF-830; Narishige) to achieve pipette resistances between 9 and 14 MΩ. Macroscopic currents were recorded at 20–22°C as acquired from cell-attached membrane patches using an Axopatch 200B patch-clamp amplifier (Molecular Devices/Axon Instruments, Sunnyvale, CA, USA). All voltage signals were generated and data were acquired with the use of an Axon Digidata 1200 A/D converter in conjunction with pClamp v10.3 software (Molecular Devices/Axon Instruments). Recordings were filtered at 2 kHz and digitized at 2–5 kHz. Typically, patches were held (V_h) at −90 mV and stepped to a depolarizing potential of +40 mV (V_c) using a pulse duration (P_d) of 1000 ms and an inter-pulse interval of 60 s. Pipettes were tip-filled with pipette solution and back-filled with MgTx, QDs, or the QD-MgTx conjugate to allow within-patch comparison of the effect of the inhibitor, nanoparticle, or conjugate, respectively.

Electrophysiological records were analyzed using Origin v8.0 (Microcal; Borland International, Scotts Valley, CA, USA), Excel v2013 (Microsoft Office, Redmond, WA, USA), and Prism 6 (Graph Pad, La Jolla, CA, USA). Patches were allowed to stabilize for 3–5 sweeps following patch formation and to release K*v* channels from an inactivated state. Following stabilization (taken as Time 0), peak current amplitude was measured (I_i, initial current) and then normalized as I_i/I_n (I_n, current at time n) to compare change in peak current amplitude over time across experiments. In experiments for which step depolarization over time and channel conductance measurements were acquired for the same cell, patches were first stimulated with a control conductance protocol (V_c = −90 mV, P_d = 50 ms, stepped to final V_c = +10 mV, in 5 mV increments) upon seal stabilization, then monitored for peak current amplitude over time (I_i/I_n) for 25 min (min), and then restimulated with the conductance protocol. In this manner, using the control tip-filled solution, and back-filled pore inhibitor, nanoparticle, or conjugate, paired within-cell measurements could be achieved for both peak current amplitude (including kinetics) as well as channel conductance. Fitting parameters for inactivation and deactivation kinetics were as previously described (Cook and Fadool 2002).

Olfactory bulb slice electrophysiology

Mice (postnatal 21–35 days C57BL/6J) were anesthetized between 10:00 am and 12:00 pm by inhalation of isoflurane (see Ethics section), quickly decapitated, and then the OBs were exposed by removing the dorsal and lateral portions of the skull between the lambda suture and the cribriform plate. The OBs were harvested and 300 μm coronal sections of the OBs were prepared using oxygenated sucrose-modified ACSF solutions during vibratome sectioning (Vibratome/Leica Model 1000, Wetzlar, Germany), as previously described (Fadool *et al.* 2011; Thiebaud *et al.* 2016). Slices were maintained at 20–22°C in an interface chamber (Krimer and Goldman-Rakic 1997) until recorded. OB slices were recorded in a continuously perfused (1 mL/min; Ismatec, Wertheim, Germany), submerged-slice recording chamber (RC-26; Warner Instruments, Hamden, CT, USA) with ACSF at 20–22°C. Slices were visualized at 10× and 40× using an Axioskop 2FS Plus microscope (Carl Zeiss Microimaging, Inc.) equipped with infrared detection capabilities (Dage MT1, CCD100; Michigan City, IN, USA). Electrodes were fabricated from borosilicate glass (#1405002; Hilgenberg, Mansfield, Germany) to a pipette resistance range from 4 to 7 MΩ. Following the determination of spike threshold, cells were stimulated with a long, peri-threshold current step (typically ranging from 5 to 50 pA) for 5000 ms every 10 s to acquire spike frequency data under ASCF conditions (Control). After the acquisition of a minimum of 10 min of recording, the bath was switched to QDs in ASCF (QD) and spike firing frequency was acquired using the same current injection for 10 min. Finally, the bath was switched a third time to apply MgTx-conjugated QDs (QD-MgTx) to the slice and the spike firing frequency was again acquired for a minimum of 10 min. Final working concentration of QD-MgTx added to the bath for these slice experiments was calculated to be 10 nM using a conjugate valence of 15.

Immunocytochemistry and QD binding

HEK293 cells were grown on glass coverslips (#12-545-90; Fisher Scientific) and were transfected with GFP-Kv1.3 cDNA at confluency. Forty-eight hours post-transfection, cells were washed 1× with PBS and 1× with HEK293 bath solution to ensure that channels were in an open state such that QD-MgTx could bind the open pore of the channel. Cells were then incubated with the QD-MgTx conjugate (100 nM with respect to the QD) for 45 min, washed 2× with PBS, and then were fixed with 3% formaldehyde (#BP531-25; Fisher Scientific). The coverslips were mounted for imaging using a mounting agent containing 4′,6-diamidino-2-phenylindole. Slides were viewed on an inverted Nikon Eclipse Ti Microscope outfitted with a Xe lamp and a color coolSNAP HQ2 CCD Camera (Nikon, Melville, NY, USA). A set of filter cubes (Chroma Technology, Rockingham, VT, USA) were used to detect 4′,6-diamidino-2-phenylindole (340–380 nm excitation/435–485 nm emission), QD (532–587 nm excitation/608–683 nm emission), and GFP (450–490 nm excitation/500–550 nm emission).

Statistical analyses

Kv1.3 peak current amplitude, channel inactivation (J_{inact}) and deactivation (J_{deact}) kinetics, voltage at half- activation ($V_{1/2}$), and slope of voltage dependence (κ) were measured prior and subsequent to application of MgTx, QD, or QD-MgTx, respectively. Each biophysical property was analyzed in the form of non-normalized data by paired *t*-test or percentage change using Arcsin transformation to determine any statistical difference in K*v* channel function in the presence of the pore blocker, nanoparticle, or conjugate at the 25 min time point (T_{25}) compared with that at the

start of the recording (T_0). The percent inhibition of Kv1.3 current by 1 nM MgTx retained over time at 20–22°C was analyzed using non-normalized data by one-way, blocked-factorial (repeated measures) analysis of variance (ANOVA) using time as the factor with a Bonferroni's *post hoc* comparison to designate significant difference. For comparisons of change in current–voltage (I–V) relationship following application of MgTx, QD, or QD-MgTx, a blocked-factorial design, two-way ANOVA was performed with voltage and inhibitor treatment condition as factors with a Bonferroni's *post hoc* comparison. All reported values are mean ± standard error of the mean (SEM) with indicated sample size (n) being the number of cell recordings. Significantly different means were calculated at the 95% confidence level or $\alpha \leq 0.05$, unless otherwise noted.

Results

MgTx can be efficiently coupled to quantum dots

The QDs were conjugated to MgTx peptide using a EDC/NHS condensation reaction (Fig. 1a). The conjugate with a valence of 15 was used in all immunocytochemistry and electrophysiology experiments. Following conjugation, QD-MgTx retained known QD absorption and emission properties (Fig. 1b and c). The generated QD-MgTx product was bath incubated for 45 min with GFP-Kv1.3- or $pcDNA_3$-transfected HEK293 cells to explore the degree of colocalization of the channel with the peptide-conjugated QD. As shown in Fig. 1d, QD-MgTx conjugate labeling was visualized (panel iv) in GFP-Kv1.3-transfected cells (panels i–vi). However, QD-MgTx conjugate labeling was absent (panel x) in $pcDNA_3$-transfected cells (panels vii–xii). Moreover, when MgTx was not bound to the QD, GFP-Kv1.3-transfected cells also remained unlabeled (panels xiii–xviii). The QD signal showed colocalization with the GFP-labeled Kv1.3 channels (panels v–vi) indicating the binding of QD-MgTx to the Kv1.3 channels. The inhomogeneous signal of GFP is attributed to the heterogeneous expression of GFP-labeled Kv1.3 channels in transfected HEK293 cells as opposed to a stable transfection condition.

QD-MgTx inhibits Kv1.3 current on a slower time course than that of MgTx alone

The kinetics of margatoxin binding is well characterized and has been shown to have a slow K_{on} of 10 min and an even slower rate of dissociation with a K_{off} of 2 h (Garcia-Calvo *et al.* 1993; Knaus *et al.* 1995). Owing to its slow binding properties, it was feasible to tip-fill the patch pipette with control ACSF and back-fill the pipette with MgTx or QD-MgTx to achieve basal current properties for a paired statistical design (within patch). Because MgTx binds the external face of the vestibule and has a rate of dissociation that would exceed the course of a typical patch recording, no attempt to dialyze the pipette or wash out of binding was attempted. Using this approach, both MgTx and the QD-MgTx conjugate were able to inhibit outward current flow in Kv1.3-transfected HEK293 cells within a 25 min period (Fig. 2a–e; two-way mixed-design ANOVA using time as a factor, $F(3, 88) = 62.98$, $p \leq 0.001$, and using treatment as a factor, $F(3, 88) = 7.019$, $p \leq 0.001$; Bonferroni's *post hoc* test significantly different across time for MgTx and QD-MgTx, $p \leq 0.001$). The mean percent inhibition by QD-MgTx was less than that of MgTx alone (79 ± 3.3%, $n = 16$ for MgTx vs. 66 ± 2.5%, $n = 36$ for QD-MgTx, Arcsine Percentage Student's t-test, $p < 0.05$). For patches treated with MgTx alone, 50% of the outward current was inhibited within 10.9 ± 1.1 min ($n = 16$) following patch stabilization (Fig. 2a and b). The inhibition of current was slower in patches treated with QD-MgTx, whereby it took 15.4 ± 1.2 min ($n = 36$) to achieve the same level of channel block (Student's t-test, $p \leq 0.0255$; Fig. 2c and d). Regardless of the inhibition kinetics, within the 25 min recording block, both MgTx and QD-MgTx significantly decreased peak current amplitude in Kv1.3-transfected cells (Fig. 2e; significantly different T_0 vs. T_{25}, two-way ANOVA using time as a factor; $F(3, 88) = 62.98$, $p \leq 0.0001$). The QDs alone did not elicit a loss of voltage-activated currents (Fig. 2e) or change the kinetics of inactivation or deactivation of the channel (Table 1), which infers that the particle itself did not occlude the channel non-selectively or modify its biophysical properties. We also explored the heat stability of MgTx (Fig. 2f) along with several venom-based and small molecule peptide inhibitors including Pap-1 and Shk-186 (Schmitz *et al.* 2005; Upadhyay *et al.* 2013; Koshy *et al.* 2014). Pap-1 was no longer an effective Kv1.3 inhibitor following heat exposure (33°C for 12 h retained < 10% inhibition, $n = 5$), and was no longer studied. Shk-186 (10 nM) exhibited heat stability (33°C for 48 h retained > 90% current inhibition, $n = 16$). MgTx retained the ability to inhibit Kv1.3 current after heat exposure for up to 2 days (Fig. 2f; significantly different from control, Kruskal–Wallis non-parametric ANOVA, Kruskal–Wallis Statistic = 34.57, $p \leq 0.0001$, $n = 5$–19).

QD-MgTx conjugate selectivity across *Shaker* family members

MgTx has been demonstrated to be a potent inhibitor for Kv1.3, but it can also block other K*v* family members at higher concentrations (Knaus *et al.* 1995; Bartok *et al.* 2014). Because a systematic study has not been reported using K*v* channels expressed in HEK293 cells, we first quantified the ability of MgTx to inhibit voltage-activated currents from Kv1.1–Kv1.7 family members. The same single-step depolarizing voltage was applied as in Fig. 2, using an identical recording strategy. Representative voltage-activated currents are shown for select time (T) points following patch stability (Fig. 3a). At a concentration of 1 nM, MgTx had no significant inhibitory effect on voltage-activated currents for Kv1.1, 1.4, 1.5, 1.6, or 1.7 (Fig. 3b, Mann–Whitney U, non-parametric paired t-test, $p \geq 0.05$,

n = 7–19). However, both Kv1.2 and Kv1.3 were inhibited by MgTx at this concentration (Fig. 3b, Mann–Whitney U, non-parametric paired t-test, p = 0.0013 for Kv1.2, n = 6–7; p = 0.0001 for Kv1.3, n = 16–18). Conjugation of the peptide inhibitor to QDs (QD-MgTx) did not alter this pattern of selectivity across the Kv family members (Fig. 4).

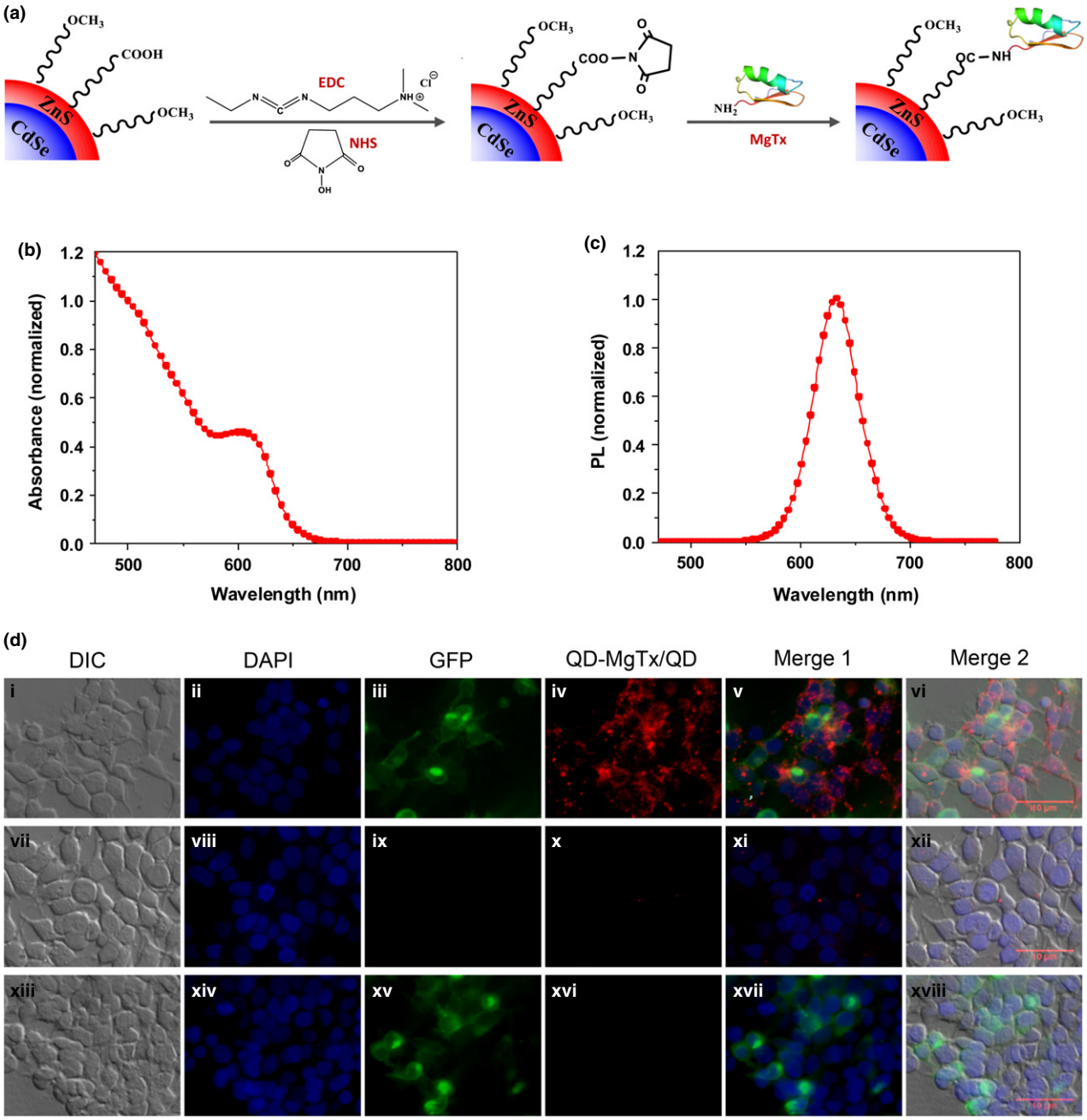

Fig. 1 CdSe–ZnS core-shell quantum dots (QDs) can be bound to margatoxin (MgTx). (a) Schematic representation showing the EDC/NHS coupling of MgTx to carboxy functionalized QDs. CdSe–ZnS over-coated fluorescent QDs containing a dihydrolipoic acid-polyethylene glycol [Dihydrolipoic acid (DHLA)-PEG] ligand terminated with 90% methoxy and 10% carboxy functional groups were bound to MgTx. Carbodiimide cross-linker chemistry (EDC) was used to couple amine groups of MgTx with the carboxy groups of the QDs. (b) Absorption and (c) emission spectra of QDs after ligand exchange. (d) Photomicrograph images of Human Embryonic Kidney 293 (HEK293) cells transfected with GFP-tagged Kv1.3 (panels i–vi and xiii–xviii) or pcDNA$_3$ vector (panels vii–xii) and incubated with QD-MgTx (panels i–xii) or QD (panels xiii–xviii). DIC, differential interference contrast; DAPI, 4′,6-diamidino-2-phenylindole nuclear stain; GFP, green fluorescent protein excitation wavelength; QD/QD-MgTx, QD excitation wavelength; Merge 1 = green, blue, and red channels merged; Merge 2 = green, blue, red, and DIC channels merged; Scale bar = 10 μm.

Whereas the mean percent inhibition observed for patches recorded from Kv1.3-transfected cells was less under peptide-conjugated conditions than for that of MgTx alone (Fig. 2e and f; Fig. 3b, 66% QD-MgTx vs. 79% MgTx), inhibition for patches recorded from Kv1.2-transfected cells was not affected by conjugation (57 ± 8%, $n = 8$ for QD-MgTx vs. 63 ± 6%, $n = 7$ for MgTx alone, Arcsin Percentage Student's t-test, $p \geq 0.05$; Fig. 3b; Fig. 4b). Peak

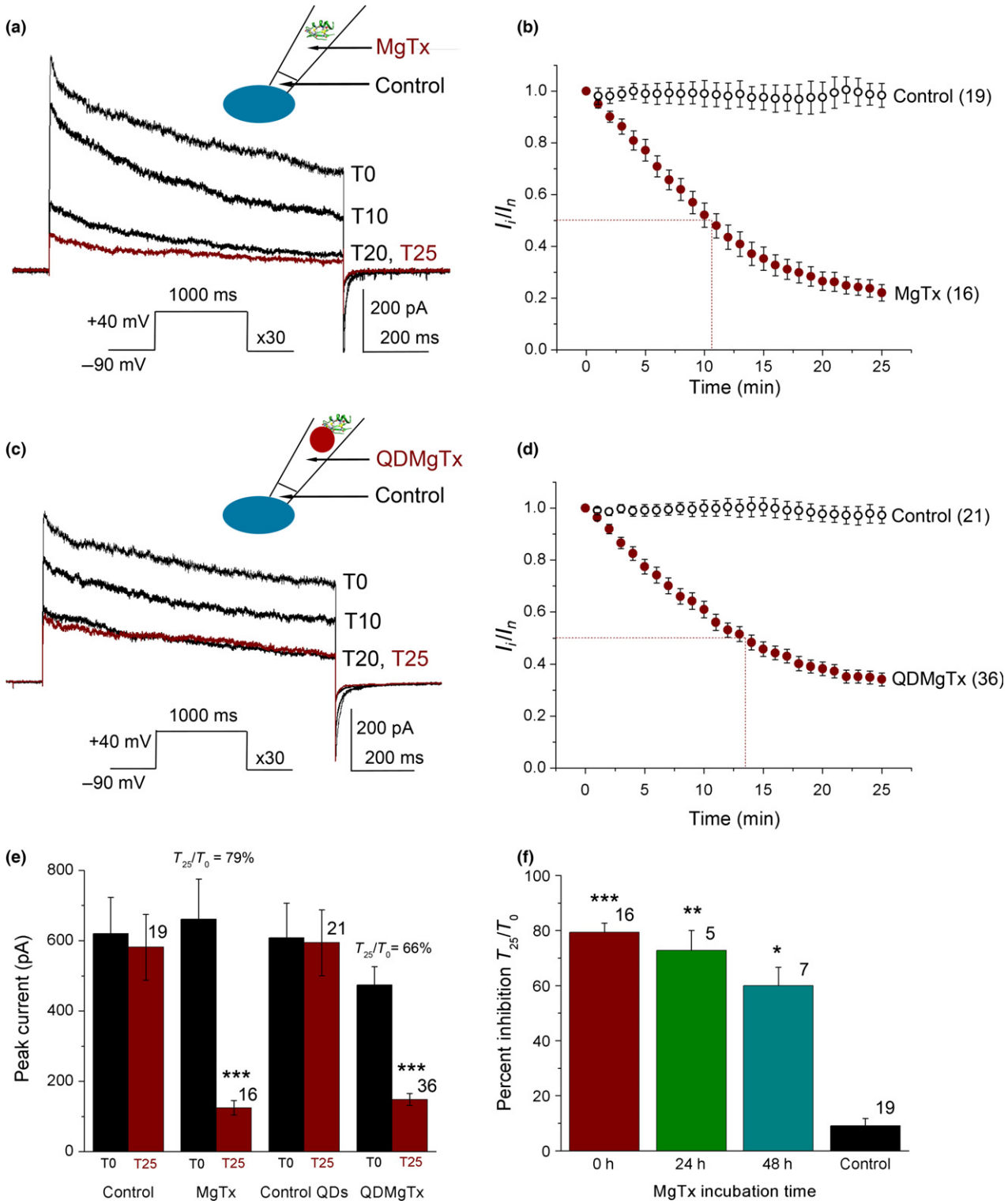

current magnitude of Kv1.1, Kv1.4, Kv1.5, and Kv1.6 was not significantly decreased either with time (control pipette solution) or with back-fill of either MgTx or QD-MgTx (Fig. 3c; Fig. 4c; paired *t*-test, $p \geq 0.05$, $n = 6$–8). Peak current magnitude of Kv1.2 and Kv1.3 was not significantly decreased with time (control HEK pipette solution), but were significantly decreased with back-fill of either MgTx or QD-MgTx (Fig. 3c; paired *t*-test, Kv1.2, $p = 0.0122$, $n = 7$; Kv1.3, $p = 0.0001$, $n = 16$; and Fig. 4c; paired *t*-test, Kv1.2, $p = 0.0278$, $n = 7$; Kv1.3, $p = 0.0001$, $n = 36$).

MgTx shifts the activation voltage and slope of voltage sensitivity without changing voltage at half-activation in Kv1.3-transfected HEK 293 cells

Because MgTx interacts with the pore vestibule, it is conceivable that properties of voltage sensing along the S4 transmembrane domain might also be affected. Mutations in the hydrophobic pore-forming region (H5) unique to K*v* channels have been found to shift half-activation or the voltage dependence of activation (Yool and Schwarz 1991; Becker *et al.* 1996; del Camino *et al.* 2000). This suggests that select pore residues may interact with the voltage sensor, the permeating ion affects the channel's own gating, or S6 structural changes in the form of a bend can modify activation gating. To study whether binding of MgTx in the pore affected voltage properties, we examined the I–V relation following peptide interaction as well as conductance properties calculated from tail currents elicited from brief step depolarizations (Fig. 5a). As shown in Fig. 5b, the I–V relation was stable over the 25 min recording interval when the pipette was tip- and back-filled with control solution (two-way mixed repeated measures ANOVA, $F(1, 84) = 1.558$, $p = 0.1143$). When the pipette was switched to contain a back-fill of MgTx, however, the activation voltage strongly shifted by as much as 30 mV, prominently affecting the I–V relation between the −60 and 0 mV window (Fig. 5e; two-way mixed repeated measures ANOVA, $F(1, 70) = 3.974$, $p = 0.0001$, Bonferroni's *post hoc* test, 0 mV, $p = 0.05$; −10 mV, $p = 0.001$; −20 to 30 mV, $p = 0.0001$; and −40 mV, $p = 0.001$) while decreasing the peak current amplitude above 10 mV (Fig. 5c; two-way mixed repeated measures ANOVA, $F(1, 70) = 8.227$, $p = 0.0001$, Bonferroni's *post hoc* test, 10 mV, $p = 0.001$; 20–40 mV, $p = 0.0001$). Interestingly, the voltage at half-activation appears to have a modest left shift over time of the recording under control conditions (Fig. 5f; Student's *t*-test, $p \leq 0.0042$, $n = 7$), which is absent when MgTx is incorporated into the back-fill (Fig. 5g; Student's *t*-test, $p = 0.4986$, $n = 7$). While there is no significant change in the $V_{1/2}$ for the residual current following MgTx application, there is a significant flattening of the relation and a great loss of voltage dependence as indicated by the slope of the voltage dependence (MgTx: T_0, $\kappa = 5.0$ vs. T_{25}, $\kappa = 19.58$; Student's *t*-test, $p \leq 0.05$; Fig. 5g). The steepness of the voltage dependence over time by comparison under control solutions was unchanged (Control: T_0, $\kappa = 5.4$ vs. T_{25}, $\kappa = 4.31$; Student's *t*-test, $p \geq 0.05$; Fig. 5f). This series of experiments exploring the I–V relation and channel conductance was repeated, but substituting the QD-MgTx conjugate (Fig. 6). Addition of

Table 1 Rate of inactivation and deactivation following application of QDs

	Control ACSF	QD
$T_{inact}T_0$ (ms)	791.5 ± 117.4	783.4 ± 168.7
$T_{inact}T_{25}$ (ms)	852 ± 98.2	753.6 ± 104.4
T_{deact} T_0 (ms)	20.1 ± 4.6	21.7 ± 7.0
$T_{deact}T_{25}$ (ms)	22.4 ± 2.6	23.5 ± 6.6

Mean ± SEM inactivation and deactivation rate (τ) for Kv1.3 currents elicited by a step depolarization from $V_h = -90$ to $V_c = +40$ during tip pipette perfusion of artificial cerebral spinal fluid (ACSF) or QDs over the recording period; T_0 (time 0)–T_{25} (time 25). Neither ACSF nor QD perfusion elicited a change in the T_{inact} or the T_{deact} overtime (Paired *t*-test, $p > 0.05$, $n = 5$–6 patches). The T_{inact} and the T_{deact} properties were not significantly different (NS) at the end of the recording (T_{25}) when comparing ACSF versus QD perfusion (Student *t*-test, $p > 0.05$, $n = 5$–6 patches). T_{inact} = inactivation time constant, T_{deact} = deactivation time constant.

Fig. 2 Time course and magnitude of Kv1.3 inhibition by MgTx versus QD-MgTx. (a) Representative cell-attached patch recording of a HEK293 cell transfected with Kv1.3 and monitored for voltage-activated currents at indicated time (T) points in minutes (min). The pipette was tip-filled with control patch solution (Control) and back-filled with margatoxin (MgTx) to facilitate a within-cell current analysis following perfusion of MgTx to the cell surface. Patches were held at −90 mV (V_h) and stepped to a +40 mV depolarizing step (V_c) for a pulse duration (P_d) of 1000 ms; inter-pulse interval (IPI) = 60 s. (b) Line graph of the normalized peak current amplitude (I_i = current initial; I_n = current at n time point) for a population of recordings as in (a) that were tip-filled with control patch solution and back-filled with control patch solution (Control) or margatoxin (MgTx). Values represent mean ± SEM. with number of patches in parenthesis. Dotted line = time to half-maximum inhibition. (c and d) Same as (a and b) but for quantum dots conjugated to MgTx (QD-MgTx). Control = unconjugated QDs. (e) Bar graph of the mean peak current amplitude at time 0 (T_0) versus time 25 (T_{25}) for unconjugated (QDs) and margatoxin-conjugated quantum dots (QD-MgTx). Two-way mixed-design analysis of variance (ANOVA) using time as a factor; Bonferroni's *post hoc* test, ***Significantly different for MgTx and QD-MgTx, $p \leq 0.001$. (f) Bar graph of the percent current inhibition evoked by back-fill of MgTx incubated at 33°C for indicated time periods versus recordings without the inhibitor (Control). Significantly different from control, Kruskal–Wallis non-parametric ANOVA, $p \leq 0.0001$, $n = 5$–19. *Post hoc* test, ***$p \leq 0.001$, **$p \leq 0.01$, *$p \leq 0.05$. (e and f) Values represent mean ± SEM, sample size = number of patches for this and subsequent figures.

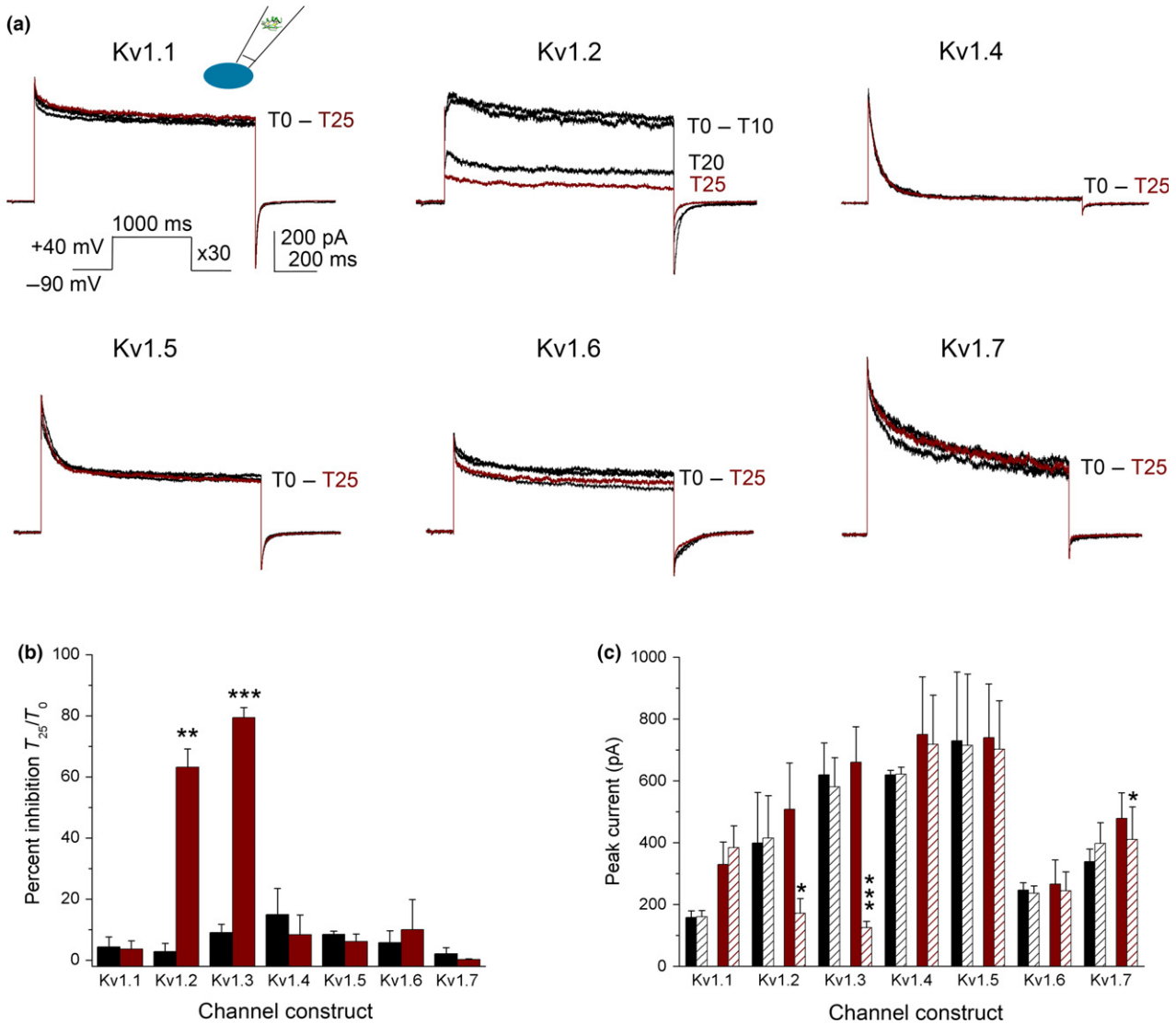

Fig. 3 MgTx selectivity across *Shaker* family members. (a) Representative cell-attached patch recording of a HEK293 cell transfected with a K*v* family member as noted and monitored for voltage-activated currents at indicated time (T) points (0, 10, 20, and 25 min). Voltage-stimulation protocol, pipette configuration, and notations as in Fig. 2. (b) Bar graph of percent current inhibition evoked by back-fill of MgTx (red) versus that of control patch solution (black). Mann–Whitney *U*, non-parametric paired *t*-test, $^{**}p = 0.0013$, $^{***}p = 0.0001$. (c) Bar graph of peak current amplitude per channel construct for patches at T_0 (solid bar) versus T_{25} (stripped bar) where recordings were made by back-fill of control patch solution (black) or MgTx (red). Paired *t*-test, $^{*}p = 0.0122$ (Kv1.2), $^{***}p = 0.0001$ (Kv1.3), $^{*}p = 0.0250$ (Kv1.7). (b and c) Sample size of each experiment = 7–19 depending upon construct.

the QD dampened the shift in activation voltage observed with MgTx approximately 20 mV, where it affected the I–V relation in the −40 to −20 mV window (Fig. 6e; two-way mixed repeated measures ANOVA, $F(1, 224) = 3.701$, $p = 0.0001$, Bonferroni's *post hoc* test, 0 to −10 mV, $p = 0.05$; −20 mV, $p = 0.0001$; −30 mV, $p = 0.01$; and −40 mV, $p = 0.05$) while decreasing the peak current amplitude above −10 mV (Fig. 6c; two-way mixed repeated measures ANOVA, $F(1, 224) = 24.09$, $p = 0.0001$, Bonferroni's *post hoc* test, −10 mV, $p = 0.05$; 0–40 mV, $p = 0.0001$). Addition of the QD to control solutions similarly caused a left shift in $V_{1/2}$ previously observed as a time-dependent change in recording (Fig. 6f vs. Fig. 5f; Student's *t*-test, $p \leq 0.007$, $n = 8$). Likewise, substitution of the QD-MgTx conjugate for MgTx similarly flattened the Boltzmann relation of the conductance curve and lessened the steepness of the voltage dependence without modifying the $V_{1/2}$ (Fig. 6g vs. Fig. 5g; QD-MgTx: T_0, $\kappa = 5.0$ vs. T_{25}, $\kappa = 9.8$; Student's *t*-test, $p \leq 0.05$; $V_{1/2}$ not significantly different, Student's *t*-test, $p = 0.3794$, $n = 17$).

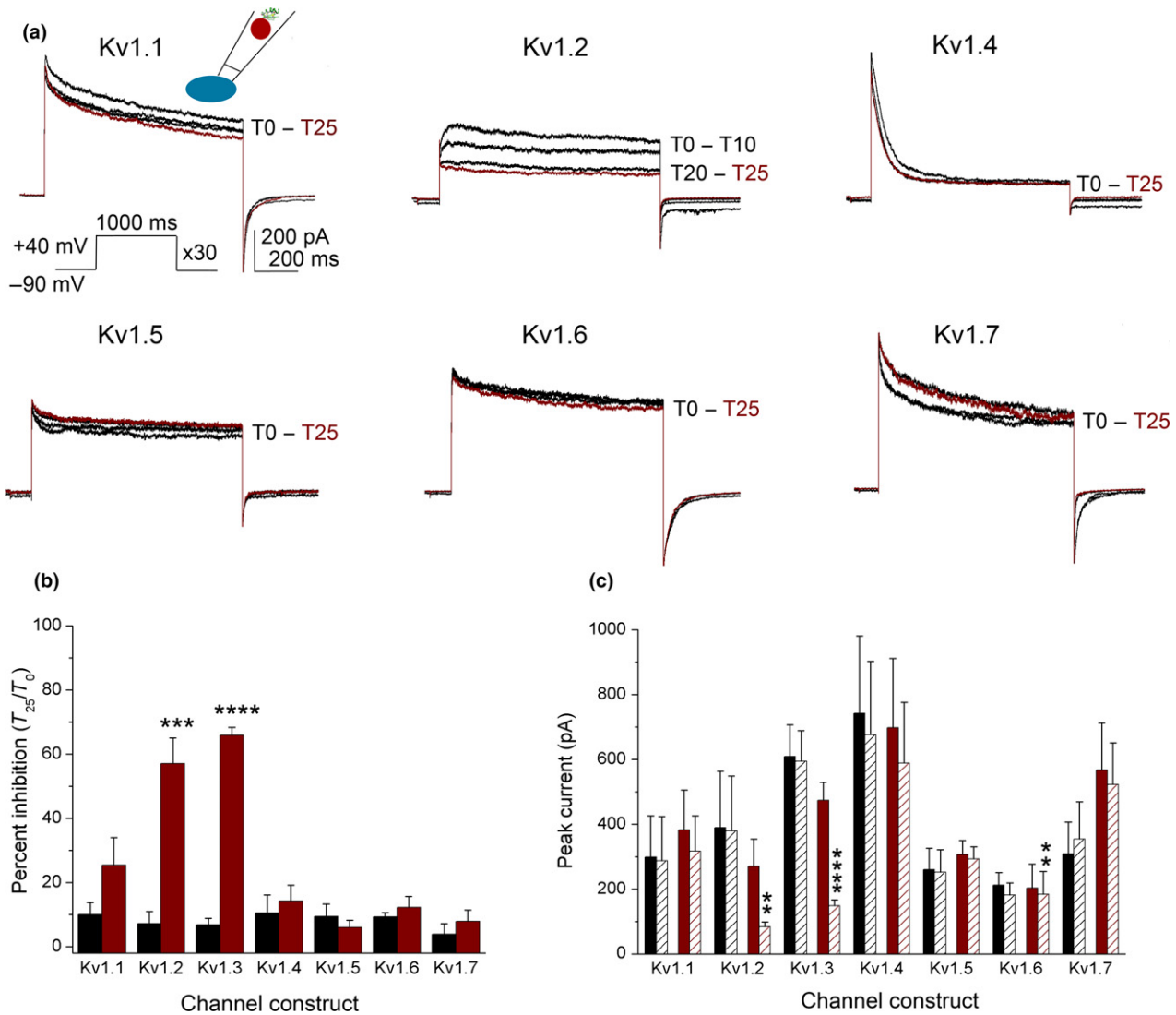

Fig. 4 QD-MgTx conjugate selectivity across *Shaker* family members. Same as Fig. 3 but substituting QD-MgTx for the back-fill of MgTx and using unconjugated QDs for the back-fill of control patch solution. Notations and statistical analysis same as Fig. 3. Sample size = 21 to 36 depending upon construct. (b) Mann–Whitney *U*, non-parametric paired *t*-test, ***$p = 0.0003$, ****$p = 0.0001$. (c) paired *t*-test, **$p = 0.0278$, ****$p = 0.0001$.

QD-MgTx enhances mitral cell action potential firing frequency in olfactory bulb slices

The olfactory bulb (OB) expresses a cadre of K*v* family members including 1.2, 1.3, and 1.4 (Kues and Wunder 1992; Wang *et al.* 1994; Fadool and Levitan 1998; Fadool *et al.* 2004). Within the neural lamina of the OB, the major output neuron to relay olfactory coding information to higher cortical regions is the mitral cell (MC). Based on pharmacological sensitivity to MgTx and Shk-186 as well as electrophysiological characterization using Kv1.3$^{-/-}$ mice, it is estimated that 60–80% of the outward current in MCs is carried by the Kv1.3 channel (Fadool and Levitan 1998; Colley *et al.* 2004; Fadool *et al.* 2004, 2011). Targeting MCs within the OB neurolamina as an *in situ* target for QD-MgTx, we anticipated an increase in action potential (AP) firing frequency in response to bath application of the peptide conjugate (Fig. 7a). Indeed, QD-MgTx significantly increased the AP firing frequency over that of control ACSF, and QDs alone did not change the AP firing compared to that of control ACSF (Fig. 7c; one-way repeated measures ANOVA, $F(2, 14) = 11.82$, $p = 0.0041$, Bonferroni's *post hoc* test, Control vs. QD – $p \geq 0.05$; QD vs. QD-MgTx – $p \leq 0.05$; Control vs. QD-MgTx – $p \leq 0.001$). Further spike analysis demonstrated that QD-MgTx decreased the pause duration between AP trains (QD; 1708.6 ± 44.5 ms vs. QD-MgTx; 456.8 ± 38.7 ms, Student's *t*-test, $p \leq 0.0001$,

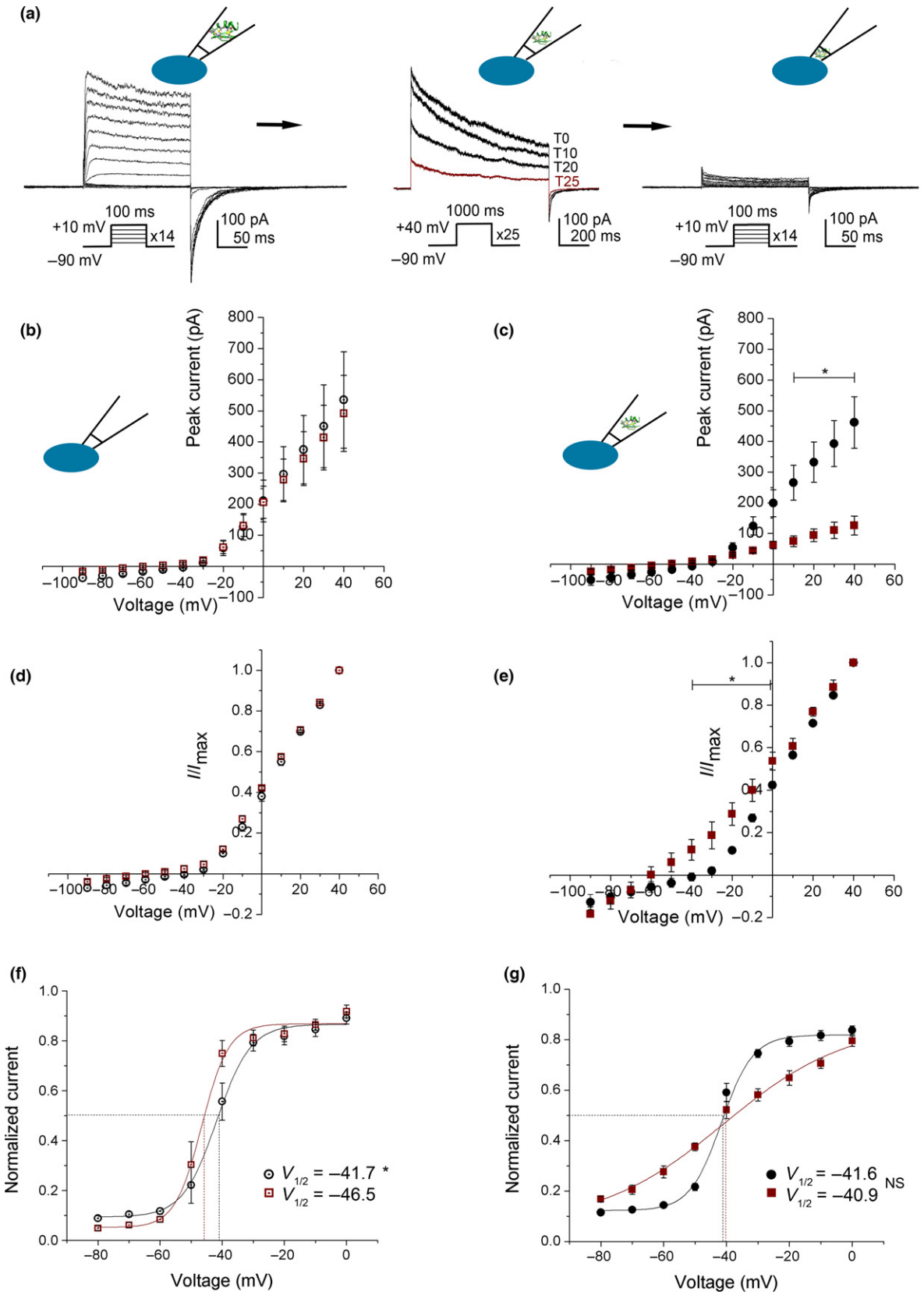
(a)
100 ms
+10 mV
x14
–90 mV
100 pA
50 ms
T0
T10
T20
T25
1000 ms
+40 mV
x25
100 pA
200 ms
100 ms
+10 mV
x14
–90 mV
100 pA
50 ms
(b)
Peak current (pA)
Voltage (mV)
(c)
Peak current (pA)
*
Voltage (mV)
(d)
I/Imax
Voltage (mV)
(e)
*
I/Imax
Voltage (mV)
(f)
Normalized current
V1/2 = –41.7 *
V1/2 = –46.5
Voltage (mV)
(g)
Normalized current
V1/2 = –41.6 NS
V1/2 = –40.9
Voltage (mV)

Fig. 5 MgTx shifts the activation voltage and slope of voltage sensitivity. (a) Representative recording protocols for a HEK293 cell transfected with Kv1.3 and monitored for voltage-activated currents using a conductance protocol to visualize tail currents upon seal stabilization (left), then a depolarizing step protocol for 25 min (center), followed by a final conductance protocol (right). Conductance protocol, V_h = −90 mV while stepped to V_c of +40 mV in 10 mV increments, P_d = 100 ms, IPI (interpulse interval) = 10 s. Depolarizing protocol = same as Fig. 2. Current–voltage relationship for a population of patches where peak current amplitude at T_0 (black ○/black ●) is plotted compared with T_{25} (red ○/red ●) for recordings tip-filled and back-filled with (b) control patch solution or (c) MgTx. Two-way mixed repeated measures ANOVA, (b) NS different, (c) *= significantly different, 10 mV, p = 0.001; 20–40 mV, p = 0.0001. (d and e) Same as (b/c) but currents are normalized to that at the final V_c (+40 mV) to standardize recordings across individual patches (I/I_{max}). Two-way mixed repeated measures ANOVA, (d) NS different, (e) *= significantly different, 0 mV, p = 0.05; −10 mV, p = 0.001; −20 to 30 mV, p = 0.0001; and −40 mV, p = 0.001. (f and g) A population of patches stimulated with the conductance protocol where normalized maximum tail currents at T_0 (black ○/black ●) is plotted compared with T_{25} (red □/red ■) for recordings tip-filled and back-filled with (f) control patch solution or (g) MgTx. Relationship was fit by the Boltzmann equation (solid line). $V_{1/2}$ = dashed line. $V_{1/2}$ compared by Student's t-test, (f) *= significantly different, p = 0.0042, n = 7. (g) = NS different, *p = 0.4986, n = 7.

n = 127) but did not affect the inter-spike interval (ISI) within the AP train (QD; 36.4 ± 1.2 ms vs. QD-MgTx; 36.5 ± 0.7 ms, Student's t-test, $p \geq 0.05$, n = 187). These patterned and intensity changes in spike firing frequency parameters in MCs are similar to what we have reported in previous studies in response to MgTx alone (Mast and Fadool 2012; Thiebaud *et al.* 2016) and with other neuromodulators that act to decrease Kv1.3 activity (Fadool *et al.* 2011).

Discussion

Our study demonstrates that it is possible to chemically conjugate a pore-blocking, venom-derived peptide to a nanoparticle and still inhibit the targeted channel without altering other biophysical properties. We have shown that QD-MgTx conjugates significantly decrease Kv1.3 current in HEK293-transfected cells and increase spike firing frequency of MCs that express native Kv1.3. Using immunocytochemical approaches, we found that the QD-MgTx conjugates bind to HEK293-transfected cells, but fail to bind in the absence of Kv1.3 cDNA. Because Kv1.3 channels retain the same biophysical properties when the vestibule is blocked with either MgTx or QD-MgTx, and the peptide itself is thermally stable for up to 48 h, we judge that the QD conjugate will be an effective tool to target and then track MgTx to Kv1.3 channels in discrete brain regions and with potential therapeutics for diseases with a well-researched role for the channel's involvement, such as multiple sclerosis, asthma, autoimmune dysfunctions, or disruption in energy homeostasis.

We have been successful in conjugating MgTx to fluorescent QDs without affecting the known biophysical properties of Kv1.3 when bound to a pore-blocking peptide. Using EDC carbodiimide chemistry, we activated carboxyl groups found on the QDs such that they would form an amide bond with basic residues found on the surface of MgTx. MgTx contains a β-sheet and an α-helix, and is stabilized by three disulfide bonds formed between Cys7–Cys29, Cys13–Cys34, and Cys17–Cys36 (Bednarek *et al.* 1994; Johnson *et al.* 1994; Chen and Chung 2014). The basic residues on MgTx's external surface form favorable electrostatic interactions, typically H-bonds or salt bridges, with acidic residues of the outer pore vestibule of Kv1.3. These interactions provide the peptide with a strong affinity for the channel, with an average distance between interacting residues of 1.7–3.3 Å (Chen and Chung 2014), and it has previously been calculated that fewer electrostatic interactions correlate with lower binding affinity (Chen *et al.* 2011). Lys28 is the most important of these residues involved with blocking Kv1.3. Lys28 is located within the second strand of the β-sheet and it disrupts the negatively charged selectivity filter of the channel upon binding the pore. When Lys28 is mutated to Ala, MgTx's ability to inhibit Kv1.3 is abolished (Anangi *et al.* 2012). Although we had no direct control over which basic residues were targeted during the conjugation to QDs, our electrophysiological data demonstrated that chemical conjugation through this methodology did not prevent MgTx from inhibiting Kv1.3, thus it is highly likely that our conjugation did not significantly affect the surface residues required to form favorable electrostatic interactions with the channel.

Albeit the QD-MgTx conjugate inhibited Kv1.3, it is interesting that the kinetics of Kv1.3 current block were slower with QD-MgTx than with that of MgTx alone. It is not certain if the time to half-inhibition was up to 3–4 min slower because the QD-conjugated peptide took longer to perfuse in the patch electrode or if the dynamics of pore interaction had been slightly changed. Given the fact that the percent inhibition by QD-MgTx was also slightly less than that of MgTx alone (66 vs. 79% inhibition) and the fact that another Kv channel's inhibition was not altered with the addition of the QD (Kv1.2) argues that the changed kinetics and efficacy of the block are more likely attributed to a minor change in the interaction of the QD-MgTx conjugated with the vestibule of Kv1.3 and not associated with pipette perfusion changes or drag of the QD. Another potential consideration is that the amines targeted for chemical conjugation likely play a role in the peptide's affinity for Kv1.3. Thus, if fewer basic residues are exposed on the surface of MgTx, its affinity for Kv1.3 might be reduced. Another possibility concerns peptide orientation.

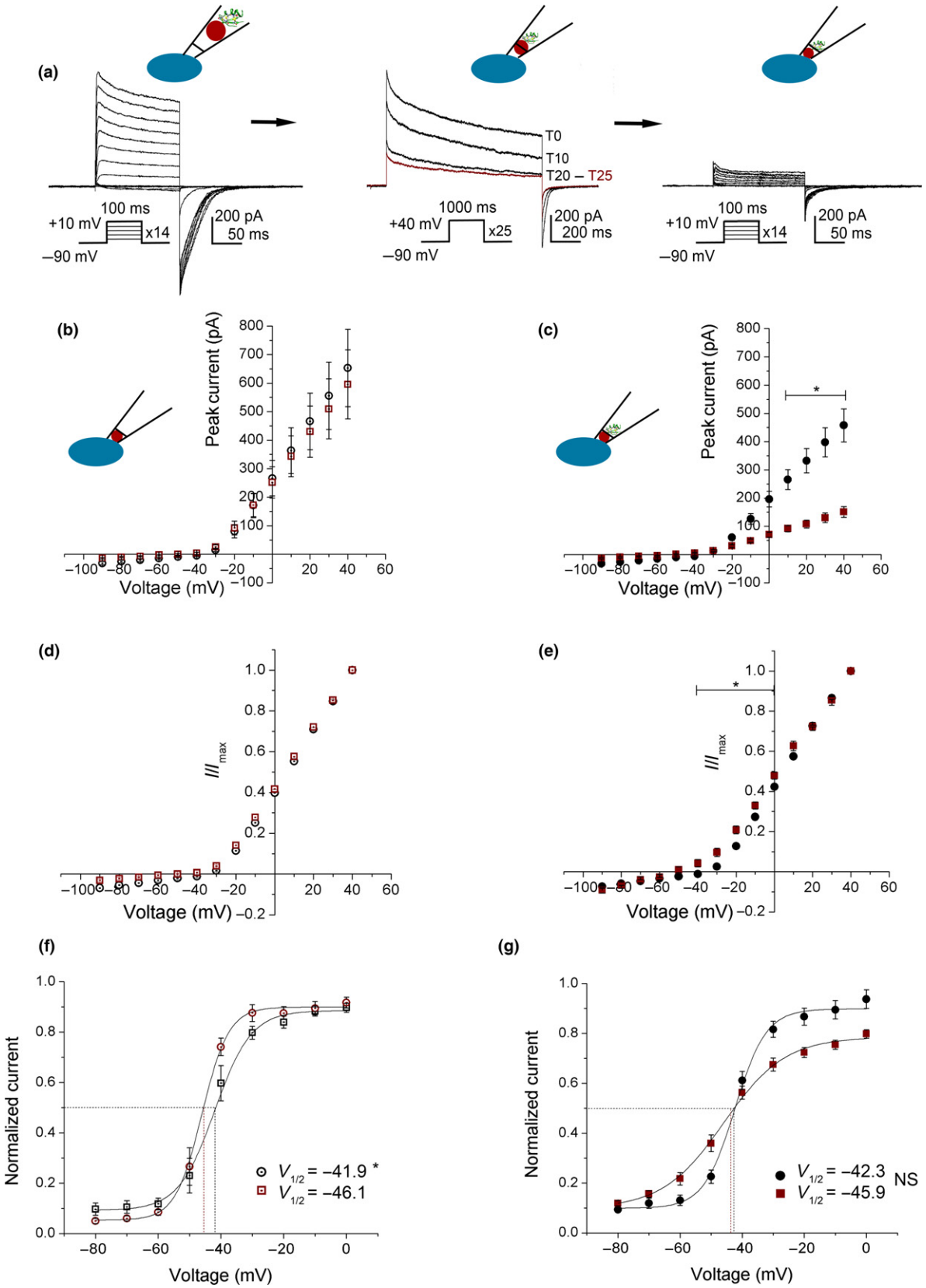
(a)
100 ms
+10 mV
x14
–90 mV
200 pA
50 ms
1000 ms
+40 mV
x25
T0
T10
T20 – T25
200 pA
200 ms
(b)
Peak current (pA)
Voltage (mV)
(c)
Peak current (pA)
*
Voltage (mV)
(d)
I/I max
Voltage (mV)
(e)
I/I max
*
Voltage (mV)
(f)
Normalized current
V1/2 = –41.9 *
V1/2 = –46.1
Voltage (mV)
(g)
Normalized current
V1/2 = –42.3 NS
V1/2 = –45.9
Voltage (mV)

Fig. 6 QD-MgTx shifts the activation voltage and slope of voltage sensitivity. Same as Fig. 5 but substituting QD-MgTx for the back-fill of MgTx and using unconjugated QDs for the back-fill of control patch solution. Notations and statistical analysis same as Fig. 5. (b) NS different, (c) *= significantly different, 10 mV, $p = 0.01$; 20–40 mV, $p = 0.001$, (d) NS different, (e) *= significantly different, 0 mV, $p = 0.05$; −10 mV, $p = 0.01$; −20 to 30 mV, $p = 0.001$; and −40 mV, $p = 0.01$, (f) *= significantly different, $p = 0.0070$, $n = 12$. (g) = NS different, $p = 0.3794$, $n = 17$.

Although a significant number of MgTx peptides must have been bound in a formation that retained their activity, it is quite possible that some of the estimated 15 bound MgTx peptides were bound in an unfavorable orientation that reduced or prevented activity. In light of this, our estimated concentration of MgTx could be less, and in turn could account for the reduced ability in inhibiting Kv1.3 or a slower time course.

Although unbound QDs have no effect on Kv1.3 current, it is possible that when MgTx is bound to QDs, it is not able to sit within the pore in a natural orientation as a result of steric constraints. In a molecular dynamics study in which His399 within the pore of hKv1.3 was mutated to Asp, the distance between interacting residues of MgTx and Kv1.3 was altered owing to changed electrostatic interactions, which reduced the strength of block (Nikouee *et al.* 2012). The Kv1.3 pore and its four voltage sensors are predicted to be 3 nm in length across the membrane (Long *et al.* 2005a,b), while the QDs used for these experiments are 12 nm in diameter with capping ligands. It is conceivable that the larger size of the QDs might reduce the average distance between interacting residues of MgTx and Kv1.3, potentially attributed to steric hindrance, altering the orientation in which the peptide sits within the pore, and reducing its strength of block.

While MgTx is widely considered a selective Kv1.3 inhibitor (K_d = 11.7 pM) (Garcia-Calvo *et al.* 1993), it has been reported to inhibit hKv1.1 and hKv1.2 at higher concentrations. At a 1 nM concentration, we did observe inhibition of rKv1.2, but not rKv1.1. This was not surprising given that the K_d for Kv1.1 is 4 nM, whereas that for Kv1.2 is 6.4 pM (Bartok *et al.* 2014). Because the goal of this work was to design a methodology for binding MgTx to a QD and to test the efficacy of the conjugate, we did not explore other concentrations of the peptide. Following binding of MgTx to the QD, the conjugate retained the observed selectively profile for MgTx, inhibiting both Kv1.3 and Kv1.2, but not Kv1.1.

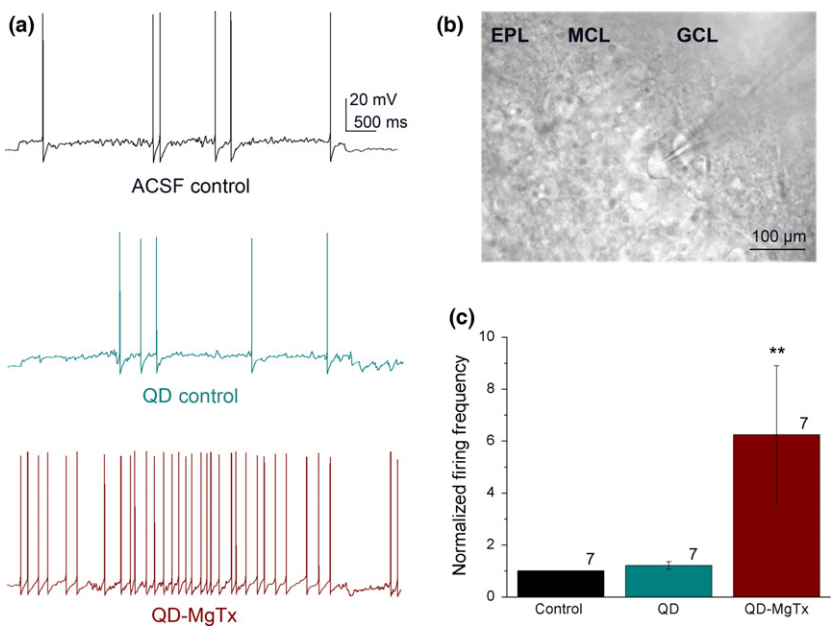

Fig. 7 Mitral cell (MC) action potential firing frequency in response to QD-MgTx. (a) Representative action potentials (APs) recorded in the whole-cell configuration in a mouse olfactory bulb (OB) slice preparation. The cell was current clamped and APs were elicited by small current injection of 25 pA. V_m = −65 mV. Spike firing frequency was first recorded under bath application of control artificial cerebral spinal fluid solution (ACSF Control), followed by unconjugated QDs (QD Control), and then MgTx-conjugated nanoparticles (QD-MgTx). (b) Photomicrograph of OB slice showing pipette position in the mitral cell neurolamina (MCL). EPL, external plexiform layer; GCL, granule cell layer. Scale bar = 100 µm. (c) Bar graph of the normalized firing frequency for a population of MCs. One-way repeated measures ANOVA, Bonferroni's *post hoc* test, **$p \leq 0.001$. Sample size = number of cell recordings.

To better understand how the QD-MgTx conjugate inhibits Kv1.3, we explored the I–V relation and conductance properties of Kv1.3 before and after block by MgTx or the QD-MgTx conjugate. When unbound MgTx inhibits Kv1.3, a strong shift in activation voltage and a clear loss of voltage dependence is observed in comparison to control solution. Similar voltage changes are observed when the QD-MgTx inhibits the channel compared to QD control, but not as strong. This is not surprising as the QD-MgTx conjugate also has a reduced ability to inhibit Kv1.3, however, this similar shift in the I–V relation further confirms the presence of MgTx on the conjugate and that the QDs alone have no effect on channel activity.

When QD-MgTx was applied to *ex vivo* OB slices, not only did it enhance AP firing frequency as anticipated but it also did so by increasing the AP burst length and decreasing the pause duration or inter-burst interval, and did not affect the inter-spike interval or ISI. This pattern of enhanced excitability of MCs is the same as that recorded following application of MgTx alone, the same as that attributed to neuromodulators that specifically reduce Kv1.3 current, and is observed in mice with Kv1.3-targeted deletion (Fadool *et al.* 2004, 2011; Tucker *et al.* 2013; Thiebaud *et al.* 2016). Even though the ability for channel inhibition by QD-MgTx versus MgTx alone demonstrates a modest difference in efficacy and kinetics (Fig. 2), this does not appear to affect the ability for enhanced AP firing in native Kv1.3-expressing neurons. It may also suggest that the degree of Kv1.3 inhibition by QD-MgTx is sufficient for depolarizing the neuron to elicit an increased AP firing frequency (6×) that is on par with that observed for MgTx alone (Thiebaud *et al.* 2016). Venom-derived ion channel inhibitors selectively inhibit their target of interest and, in our case, are able to target native Kv1.3 channels in a brain slice. Molecules like our developed QD-MgTx conjugate will be advantageous in future drug delivery studies as they will provide a means of tracking the drug molecule following delivery. The developed QD-MgTx conjugate has a similar ability of inhibiting Kv1.3 and exciting MCs of the OB. Future therapeutic interventions using intranasal delivery of QD-MgTx could be developed to enhance olfactory ability, increase metabolism, or modulate olfactory-coded information to this CNS neural network.

Acknowledgments and conflict of interest disclosure

We would like to thank Wesley Joshua Earl and James A. Warrington for routine technical assistance. We would like to thank Ms. Cheryl Pye and Mr. Brian Washburn for assistance with subcloning our channel constructs in the FSU Molecular Core Facility. We would like to thank Drs K. George Chandy and Michael Pennington for ShK-186 peptide. This work was supported by grants R01 DC013080 and F31 DC014638 from the National Institutes of Health (NIH) at the National Institute of Deafness and Communication Disorders (NIDCD) and a grant from the National Science Foundation (NSF-CHE #1508501). None of the authors have any potential sources of conflicts of interest that would influence objectivity.

All experiments were conducted in compliance with the ARRIVE guidelines.

References

Anangi R., Koshy S., Huq R., Beeton C., Chuang W. J. and King G. F. (2012) Recombinant expression of margatoxin and agitoxin-2 in Pichia pastoris: an efficient method for production of KV1.3 channel blockers. *PLoS ONE* **7**, e52965.

Armstrong C. M. (1966) Time course of TEA(+)-induced anomalous rectification in squid giant axons. *J. Gen. Physiol.* **50**, 491–503.

Armstrong C. M. (1969) Inactivation of the potassium conductance and related phenomena caused by quaternary ammonium ion injection in squid axons. *J. Gen. Physiol.* **54**, 553–575.

Bartok A., Toth A., Somodi S., Szanto T. G., Hajdu P., Panyi G. and Varga Z. (2014) Margatoxin is a non-selective inhibitor of human Kv1.3 K^+ channels. *Toxicon* **87**, 6–16.

Becker D., Dreyer I., Hoth S., Reid J. D., Busch H., Lehnen M., Palme K. and Hedrich R. (1996) Changes in voltage activatin, Cs+ sensitivity, and ion permeability in H5 mutants of the K^+ channel KAT1. *Proc. Natl Acad. Sci. USA* **93**, 8123–8128.

Bednarek M. A., Bugianesi R. M., Leonard R. J. and Felix J. P. (1994) Chemical synthesis and structure-function studies of margatoxin, a potent inhibitor of voltage-dependent potassium channel in human T lymphocytes. *Biochem. Biophys. Res. Commun.* **198**, 619–625.

Beeton C., Pennington M. W. and Norton R. S. (2011) Analogs of the sea anemone potassium channel blocker ShK for the treatment of autoimmune diseases. *Inflamm. Allergy Drug Targets* **10**, 313–321.

Biju K. C., Marks D. R., Mast T. G. and Fadool D. A. (2008) Deletion of voltage-gated channel affects glomerular refinement and odorant receptor expression in the mouse olfactory system. *J. Comp. Neurol.* **506**, 161–179.

Camerino D. C., Tricarico D. and Desaphy J.-F. (2007) Ion channel pharmcology. *Neurotherapeutics* **4**, 184–198.

del Camino D., Holmgren M., Liu Y. and Yellen G. (2000) Blocker protection in the pore of a voltage-gated K^+ channel and its structural implications. *Nature* **403**, 321–325.

Catterall W. A. (1988) Structure and function of voltage-sensitive ion channels. *Science* **242**, 50–61.

Chen R. and Chung S. H. (2014) Binding modes of two scorpion toxins to the voltage-gated potassium channel kv1.3 revealed from molecular dynamics. *Toxins. (Basel)* **6**, 2149–2161.

Chen R., Robinson A., Gordon D. and Chung S. H. (2011) Modeling the binding of three toxins to the voltage-gated potassium channel (Kv1.3). *Biophys. J* . **101**, 2652–2660.

Chhabra S., Chang S. C., Nguyen H. M. *et al.* (2014) Kv1.3 channel-blocking immunomodulatory peptides from parasitic worms: implications for autoimmune diseases. *FASEB J.* **28**, 3952–3964.

Chi V., Pennington M. W., Norton R. S. *et al.* (2012) Development of a sea anemone toxin as an immunomodulator for therapy of autoimmune diseases. *Toxicon* **59**, 529–546.

Clapp A. R., Goldman E. R. and Mattoussi H. (2006) Capping of CdSe-ZnS quantum dots with DHLA and subsequent conjugation with proteins. *Nat. Protoc.* **1**, 1258–1266.

Clyner J. (2007) Phosphate Buffer Calculator. http://www.clymer.altervista.org/buffers/phos2.html

Colley B., Tucker K. and Fadool D. A. (2004) Comparison of modulation of Kv1.3 channel by two receptor tyrosine kinases in

olfactory bulb neurons of rodents. *Receptors Channels* **10**, 25–36.

Cook N. S. (1988) The pharmacology of potassium channels and their therapeutic potential. *Trends Pharmacol. Sci.* **9**, 21–28.

Cook K. K. and Fadool D. A. (2002) Two adaptor proteins differentially modulate the phosphorylation and biophysics of Kv1.3 ion channel by SRC kinase. *J. Biol. Chem.* **277**, 13268–13280.

Fadool D. A. and Levitan I. B. (1998) Modulation of olfactory bulb neuron potassium current by tyrosine phosphorylation. *J. Neurosci.* **18**, 6126–6137.

Fadool D. A., Tucker K., Phillips J. J. and Simmen J. A. (2000) Brain insulin receptor causes activity-dependent current suppression in the olfactory bulb through multiple phosphorylation of Kv1.3. *J. Neurophysiol.* **83**, 2332–2348.

Fadool D. A., Tucker K., Perkins R., Fasciani G., Thompson R. N., Parsons A. D., Overton J. M., Koni P. A., Flavell R. A. and Kaczmarek L. K. (2004) Kv1.3 channel gene-targeted deletion produces "Super-Smeller Mice" with altered glomeruli, interacting scaffolding proteins, and biophysics. *Neuron* **41**, 389–404.

Fadool D. A., Tucker K. and Pedarzani P. (2011) Mitral cells of the olfactory bulb perform metabolic sensing and are disrupted by obesity at the level of the Kv1.3 ion channel. *PLoS ONE* **6**, e24921.

Garcia-Calvo M., Leonard R. J., Novick J., Stevens S. P., Schmalhofer W., Kaczorowski G. J. and Garcia M. L. (1993) Purification, characterization, and biosynthesis of margatoxin, a component of *Centruroides margaritatus* venom that selectively inhibits voltage-dependent potassium channels 39. *J. Biol. Chem.* **268**, 18866–18874.

Ghanshani S., Wulff H., Miller M. J., Rohm H., Neben A., Gutman G. A., Cahalan M. D. and Chandy K. G. (2000) Up-regulation of the IKCa1 potassium channel during T-cell activation. Molecular mechanism and functional consequences. *J. Biol. Chem.* **275**, 37137–37149.

Guo Z., Peng H., Kang J. and Sun D. (2016) Cell-penetrating peptides: possible transduction mechanisms and therapeutic applications. *Biomed. Rep.* **4**, 528–534.

Hagen N. A., Fisher K. M., Lapointe B., du Souich P., Chary S., Moulin D., Sellers E. and Ngoc A. H. (2007) An open-label, multi-dose efficacy and safety study of intramuscular tetrodotoxin in patients with severe cancer-related pain. *J. Pain Symptom Manage.* **34**, 171–182.

Hagen N. A., du Souich P., Lapointe B., Ong-Lam M., Dubuc B., Walde D., Love R. and Ngoc A. H. (2008) Tetrodotoxin for moderate to severe cancer pain: a randomized, double blind, parallel design multicenter study. *J. Pain Symptom Manage.* **35**, 420–429.

Hagen N. A., Lapointe B., Ong-Lam M. *et al.* (2011) A multicentre open-label safety and efficacy study of tetrodotoxin for cancer pain. *Curr. Oncol.* **18**, e109–e116.

Hermanson G. T. (2013) *Bioconjugate Techniques*, Academic Press, San Diego.

Holmes T. C., Fadool D. A. and Levitan I. B. (1996) Tyrosine phosphorylation of the Kv1.3 potassium channel. *J. Neurosci.* **16**, 1581–1590.

Isacoff E. Y., Jan L. Y. and Minor D. L. Jr (2013) Conduits of life's spark: a perspective on ion channel research since the birth of neuron. *Neuron* **80**, 658–674.

Jan L. Y. and Jan Y. N. (2012) Voltage-gated potassium channels and the diversity of electrical signalling. *J. Physiol.* **590**, 2591–2599.

Jang S. H., Byun J. K., Jeon W. I. *et al.* (2015) Nuclear localization and functional characteristics of voltage-gated potassium channel Kv1.3. *J. Biol. Chem.* **290**, 12547–12557.

Johnson B. A., Stevens S. P. and Williamson J. M. (1994) Determination of the three-dimensional structure of margatoxin by 1H, 13C, 15N triple-resonance nuclear magnetic resonance spectroscopy. *Biochemistry* **33**, 15061–15070.

Jurman M. E., Boland L. M., Liu Y. and Yellen G. (1994) Visual identification of individual transfected cells for electrophysiology using antibody-coated beads. 7. *Biotechniques* **17**, 876–881.

Kaczorowski G. J. and Garcia M. L. (1999) Pharmacology of voltage-gated and calcium-activated potassium channels. *Curr. Opin. Chem. Biol.* **3**, 448–458.

Kalia J., Milescu M., Salvatierra J., Wagner J., Klint J. K., King G. F., Olivera B. M. and Bosmans F. (2015) From foe to friend: using animal toxins to investigate ion channel function. *J. Mol. Biol.* **427**, 158–175.

Kazama I. (2015) Physiological significance of delayed rectifier K(+) channels (Kv1.3) expressed in T lymphocytes and their pathological significance in chronic kidney disease. *J. Physiol. Sci.* **65**, 25–35.

Knaus H. G., Koch R. O., Eberhart A., Kaczorowski G. J., Garcia M. L. and Slaughter R. S. (1995) [125I]margatoxin, an extraordinarily high affinity ligand for voltage-gated potassium channels in mammalian brain. *Biochemistry* **34**, 13627–13634.

Koshy S., Huq R., Tanner M. R., Atik M. A., Porter P. C., Khan F. S., Pennington M. W., Hanania N. A., Corry D. B. and Beeton C. (2014) Blocking KV1.3 channels inhibits Th2 lymphocyte function and treats a rat model of asthma. *J. Biol. Chem.* **289**, 12623–12632.

Krimer L. S. and Goldman-Rakic P. S. (1997) An interface holding chamber for anatomical and physiological studies of living brain slices. *J. Neurosci. Methods* **75**, 55–58.

Kues W. A. and Wunder F. (1992) Heterogeneous expression patterns of mammalian potassium channel genes in developing and adult rat brain. *Eur. J. Neurosci.* **4**, 1296–1308.

Kupper J. (1998) Functional expression of GFP-tagged Kv1.3 and Kv1.4 channels in HEK 293 cells. *Eur. J. Neurosci.* **10**, 3908–3912.

Lam J. and Wulff H. (2011) The lymphocyte potassium channels Kv1.3 and KCa3.1 as targets for immunosuppression. *Drug Dev. Res.* **72**, 573–584.

Leatherdale C. A., Woo W.-K., Mikulec F. V. and Bawendi M. G. (2002) On the absorption cross section of CdSe nanocrystal quantum dots. *J. Phys. Chem. B* **106**, 7619–7622.

Long S. B., Campbell E. B. and MacKinnon R. (2005a) Crystal structure of a mammalian voltage-dependent Shaker family K^+ channel. *Science* **309**, 897–903.

Long S. B., Campbell E. B. and MacKinnon R. (2005b) Voltage sensor of Kv1.2: structural basis of electromechanical coupling. *Science* **309**, 903–908.

Mast T. G. and Fadool D. A. (2012) Mature and precursor brain-derived neurotrophic factor have individual roles in the mouse olfactory bulb. *PLoS ONE* **7**, e31978.

Mast T. G., Brann J. H. and Fadool D. A. (2010) The TRPC2 channel forms protein-protein interactions with Homer and RTP in the rat vomeronasal organ. 8. *BMC Neurosci.* **11**, 61.

Mathie A., Wooltorton J. R. and Watkins C. S. (1998) Voltage-activated potassium channels in mammalian neurons and their block by novel pharmacological agents. *Gen. Pharmacol.* **30**, 13–24.

Mattoussi H., Palui G. and Na H. B. (2012) Luminescent quantum dots as platforms for probing in vitro and in vivo biological processes. *Adv. Drug Deliv. Rev.* **64**, 138–166.

Menteyne A., Levavasseur F., Audinat E. and Avignone E. (2009) Predominant functional expression of Kv1.3 by activated microglia of the hippocampus after Status epilepticus. *PLoS ONE* **4**, e6770.

Nikouee A., Khabiri M., Grissmer S. and Ettrich R. (2012) Charybdotoxin and margatoxin acting on the human voltage-gated potassium channel hKv1.3 and its H399N mutant: an experimental and computational comparison. *J. Phys. Chem. B* **116**, 5132–5140.

Nitabach M. N., Llamas D. A., Thompson I. J., Collins K. A. and Holmes T. C. (2002) Phosphorylation-dependent and

phosphorylation-independent modes of modulation of shaker family voltage-gated potassium channels by SRC family protein tyrosine kinases. 6. *J. Neurosci.* **22**, 7913–7922.

Palui G., Avellini T., Zhan N., Pan F., Gray D., Alabugin I. and Mattoussi H. (2012a) Photoinduced phase transfer of luminescent quantum dots to polar and aqueous media. *J. Am. Chem. Soc.* **134**, 16370–16378.

Palui G., Na H. B. and Mattoussi H. (2012b) Poly(ethylene glycol)-based multidentate oligomers for biocompatible semiconductor and gold nanocrystals. *Langmuir* **28**, 2761–2772.

Pineda S. S., Undheim E. A., Rupasinghe D. B., Ikonomopoulou M. P. and King G. F. (2014) Spider venomics: implications for drug discovery. *Future. Med. Chem.* **6**, 1699–1714.

Pongs O. (1992) Structural basis of voltage-gated K^+ channel pharmacology. *Trends Pharmacol. Sci.* **13**, 359–365.

Rangaraju S., Chi V., Pennington M. W. and Chandy K. G. (2009) Kv1.3 potassium channels as a therapeutic target in multiple sclerosis. *Expert. Opin. Ther. Targets.* **13**, 909–924.

Rubaiy H. N. (2016) The therapeutic agents that target ATP-sensitive potassium channels. *Acta Pharm.* **66**, 23–34.

Schmitz A., Sankaranarayanan A., Azam P., Schmidt-Lassen K., Homerick D., Hansel W. and Wulff H. (2005) Design of PAP-1, a selective small molecule Kv1.3 blocker, for the suppression of effector memory T cells in autoimmune diseases. *Mol. Pharmacol.* **68**, 1254–1270.

Sheng J., He H., Han L., Qin J., Chen S., Ru G., Li R., Yang P., Wang J. and Yang V. C. (2016) Enhancing insulin oral absorption by using mucoadhesive nanoparticles loaded with LMWP-linked insulin conjugates. *J. Control Release* **233**, 181–190.

Skibsbye L. and Ravens U. (2016) Mechanism of proarrhythmic effects of potassium channel blockers. *Card Electrophysiol. Clin.* **8**, 395–410.

Spear J. M., Koborssy D. A., Schwartz A. B., Johnson A. J., Audhya A., Fadool D. A. and Stagg S. M. (2015) Kv1.3 contains an alternative C-terminal ER exit motif and is recruited into COPII vesicles by Sec24a. *BMC. Biochem* **16**, 16.

Spencer R. H., Sokolov Y., Li H. *et al.* (1997) Purification, visualization, and biophysical characterization of Kv1.3 tetramers. *J. Biol. Chem.* **272**, 2389–2395.

Susumu K., Uyeda H. T., Medintz I. L., Pons T., Delehanty J. B. and Mattoussi H. (2007) Enhancing the stability and biological functionalities of quantum dots via compact multifunctional ligands. *J. Am. Chem. Soc.* **129**, 13987–13996.

Susumu K., Mei B. C. and Mattoussi H. (2009) Multifunctional ligands based on dihydrolipoic acid and polyethylene glycol to promote biocompatibility of quantum dots. *Nat. Protoc.* **4**, 424–436.

Thiebaud N., Johnson M. C., Butler J. L., Bell G. A., Ferguson K. L., Fadool A. R., Fadool J. C., Gale A. M., Gale D. S. and Fadool D. A. (2014) Hyperlipidemic diet causes loss of olfactory sensory neurons, reduces olfactory discrimination, and disrupts odor-reversal learning. *J. Neurosci.* **34**, 6970–6984.

Thiebaud N., Llewellyn-Smith I., Gribble F., Reimann F., Trapp S. and Fadool D. A. (2016) The incretin hormone glucagon-like peptide 1 increases mitral cell excitability by decreasing conductance of a voltage-dependent potassium channel. 72. *J. Physiol.* **594**, 2607–2628.

Toldi G., Bajnok A., Dobi D., Kaposi A., Kovacs L., Vasarhelyi B. and Balog A. (2013) The effects of Kv1.3 and IKCa1 potassium channel inhibition on calcium influx of human peripheral T lymphocytes in rheumatoid arthritis. *Immunobiology* **218**, 311–316.

Trimmer J. S. (2015) Subcellular localization of K^+ channels in mammalian brain neurons: remarkable precision in the midst of extraordinary complexity. *Neuron* **85**, 238–256.

Tucker K., Overton J. M. and Fadool D. A. (2008) Kv1.3 gene-targeted deletion alters longevity and reduces adiposity by increasing locomotion and metabolism in melanocortin-4 receptor-null mice. *Int. J. Obes. (Lond)* **32**, 1222–1232.

Tucker K., Overton J. M. and Fadool D. A. (2012a) Diet-induced obesity resistance of $Kv1.3^{-/-}$ mice is olfactory bulb dependent. *J. Neuroendocrinol.* **24**, 1087–1095.

Tucker K. R., Godbey S. J., Thiebaud N. and Fadool D. A. (2012b) Olfactory ability and object memory in three mouse models of varying body weight, metabolic hormones, and adiposity. *Physiol. Behav.* **107**, 424–432.

Tucker K., Cho S., Thiebaud N., Henderson M. X. and Fadool D. A. (2013) Glucose sensitivity of mouse olfactory bulb neurons is conveyed by a voltage-gated potassium channel 26. *J. Physiol.* **591**, 2541–2561.

Undheim E. A., Fry B. G. and King G. F. (2015) Centipede venom: recent discoveries and current state of knowledge. *Toxins. (Basel)* **7**, 679–704.

Upadhyay S. K., Eckel-Mahan K. L., Mirbolooki M. R. *et al.* (2013) Selective Kv1.3 channel blocker as therapeutic for obesity and insulin resistance. *Proc. Natl Acad. Sci. USA* **110**, E2239–E2248.

Wang H., Kunkel D. D., Schwartzkroin P. A. and Tempel B. L. (1994) Localization of Kv1.1 and Kv1.2, two K channel proteins, to synaptic terminals, somata, and dendrites in the mouse brain. *J. Neurosci.* **14**, 4588–4599.

Xie Z., Feng J., Yang W., Xiang F., Yang F., Zhao Y., Cao Z., Li W., Chen Z. and Wu Y. (2015) Human alpha-defensins are immune-related Kv1.3 channel inhibitors: new support for their roles in adaptive immunity. *FASEB. J.* **29**, 4324–4333.

Xu J., Koni P. A., Wang P., Li G., Kaczmarek L. K., Wu Y., Li Y., Flavell R. A. and Desir G. V. (2003) The voltage-gated potassium channel Kv1.3 regulates energy homeostasis and body weight 15. *Hum. Mol. Genet.* **12**, 551–559.

Xu J., Wang P., Li Y., Li G., Laczmarek L. K., Wu Y., Koni P. A., Flavell R. A. and Desir G. V. (2004) The voltage-gated potassium channel Kv1.3 regulates peripheral insulin senstivitiy 16. *Proc. Natl Acad. Sci.* **101**, 3112–3117.

Yang K. C. and Nerbonne J. M. (2016) Mechanisms contributing to myocardial potassium channel diversity, regulation and remodeling. *Trends Cardiovasc. Med.* **26**, 209–218.

Yang S., Xiao Y., Kang D., Liu J., Li Y., Undheim E. A., Klint J. K., Rong M., Lai R. and King G. F. (2013) Discovery of a selective NaV1.7 inhibitor from centipede venom with analgesic efficacy exceeding morphine in rodent pain models. *Proc. Natl Acad. Sci. USA* **110**, 17534–17539.

Yellen G. (2002) The voltage-gated potassium channels and their relatives. *Nature (London)* **419**, 35–42.

Yool J. A. and Schwarz T. L. (1991) Alteration of ionic selectivity of a K^+ channel by mutation of the H5 region. *Nature* **349**, 700–704.

Yu W. W. and Peng X. (2002) Formation of high-quality CdS and other II-VI semiconductor nanocrystals in noncoordinating solvents: tunable reactivity of monomers. *Angew. Chem. Int. Ed. Engl.* **41**, 2368–2371.

Yu F. H., Yarov-Yarovoy V., Gutman G. A. and Catterall W. A. (2005) Overview of molecular relationships in the voltage-gated ion channel superfamily. *Pharm. Exp. Therapeut.* **57**, 387–395.